Nanoscale spectroscopic origins of photoinduced tip–sample force in the midinfrared

Junghoon Jahng[a], Eric O. Potma[b,1], and Eun Seong Lee[a,1]

[a]Center for Nanocharacterization, Korea Research Institute of Standards and Science, Daejeon 34113, South Korea; and [b]Department of Chemistry, University of California, Irvine, CA 92697

Edited by Catherine J. Murphy, University of Illinois at Urbana–Champaign, Urbana, IL, and approved November 8, 2019 (received for review August 8, 2019)

When light illuminates the junction formed between a sharp metal tip and a sample, different mechanisms can contribute to the measured photoinduced force simultaneously. Of particular interest are the instantaneous force between the induced dipoles in the tip and in the sample, and the force related to thermal heating of the junction. A key difference between these 2 force mechanisms is their spectral behavior. The magnitude of the thermal response follows a dissipative (absorptive) Lorentzian line shape, which measures the heat exchange between light and matter, while the induced dipole response exhibits a dispersive spectrum and relates to the real part of the material polarizability. Because the 2 interactions are sometimes comparable in magnitude, the origin of the chemical selectivity in nanoscale spectroscopic imaging through force detection is often unclear. Here, we demonstrate theoretically and experimentally how the light illumination gives rise to the 2 kinds of photoinduced forces at the tip–sample junction in the midinfrared. We comprehensively address the origin of the spectroscopic forces by discussing cases where the 2 spectrally dependent forces are entwined. The analysis presented here provides a clear and quantitative interpretation of nanoscale chemical measurements of heterogeneous materials and sheds light on the nature of light–matter coupling in optomechanical force-based spectronanoscopy.

optically induced force | induced (image) dipole | tip-enhanced thermal expansion | nanoscale spectroscopic imaging | photoinduced force microscopy

The light–matter interaction responsible for optically induced forces has enabled imaging and manipulation of various objects at nanoscale and microscale (1–3). These optically induced forces can originate from local electromagnetic field gradients, radiation pressure, and/or thermal expansion of materials, and are sensitive to material properties such as optical (4), chemical (5), and mechanical (6) properties including chirality (7). Such optical forces are of fundamental importance in applications ranging from optical trapping (8, 9) to modern microscopy techniques (10–12). Recent efforts in microscopy through optical force detection have focused on the high-resolution capabilities of scan-probe techniques with chemical selectivity to meet a growing demand in nanoscience and nanotechnology for compositional analysis at the nanoscale. Photoinduced force microscopy (PiFM) (5, 13), photothermal-induced resonance technique (PTIR) (11, 14, 15), and peak force infrared microscopy (PFIR) (12) are prime examples of imaging techniques that probe optical forces, enabling chemically sensitive mapping of materials at the nanoscale. In addition, the light-based scan-probe approach also facilitates the study of fundamental light–matter interactions in the tip–sample junction, such as polaritonic effects in van der Waals materials (16, 17).

Both PTIR and PFIR probe the spectroscopic response of the sample by registering the thermal expansion of the material, which is in mechanical contact with the tip and in contact resonance mode. Although these latter approaches generate nanoscale maps with genuine chemical contrast, they require the tip to be in physical contact with the sample. In some cases, scanning in contact mode may pose problems and can damage the sample and the tip. Compared to the PTIR and PFIR, the recently developed PiFM operates in the noncontact/tapping mode while monitoring the photoinduced force between the tip and the sample. Theoretically, when the light illuminates the tip–sample junction, the induced dipoles in the tip and in the sample generate a coulombic force whose spectral response follows a dispersive line shape (5, 18, 19). Meanwhile, near molecular resonances, there is a temperature rise of the sample due to light absorption, which results in the thermal expansion of the sample. The spectral response of the thermal expansion follows a dissipative (absorptive) Lorentzian line shape (20, 21), as observed in PTIR and PFIR, which measure the heat exchange between light and matter.

Because the 2 interactions are sometimes comparable in magnitude with respect to the sample's optical and thermal properties, the origin of the chemical selectivity of the nanoscale spectroscopic imaging through force detection is often unclear. Moreover, specialized detection techniques such as heterodyne-detected PiFM (side-band mode), which operates in the noncontact/tapping mode and is sensitive to the surface response (22) rather than the bulk response, make it rather challenging to understand the coupling mechanism between the thermal expansion and the oscillating tip. In this work, we reveal the origin of the photoinduced force by studying each force with respect to the sample's optical and thermal properties in the midinfrared (MIR) range by implementing the PiFM. We also underline the noncontact

Significance

Photoinduced force at tip–sample junction provides nanoscale spectroscopic information with label-free and far-field background-free manner. This approach, spectronanoscopy through force detection, shows higher sensitivity and 1,000 times better spatial resolution than conventional ensemble averaged infrared microscopy, even under ambient and environmental conditions. Unfortunately, the origin of this promising photoinduced force effect is sometimes unclear because the force has 2 independent physical aspects: One is the electromagnetic effect related to induced dipoles in tip and sample, and the other one is the thermodynamic effect related to thermal heating of sample. Here, we reveal how the light illumination results in the 2 kinds of photoinduced forces at the tip–sample junction and provide quantitative interpretation of nanoscale spectroscopic measurements.

Author contributions: J.J. and E.S.L. designed research; J.J. performed research; J.J., E.O.P., and E.S.L. contributed new reagents/analytic tools; J.J., E.O.P., and E.S.L. analyzed data; and J.J., E.O.P., and E.S.L. wrote the paper.

The authors declare no competing interest.

This article is a PNAS Direct Submission.

[1]To whom correspondence may be addressed. Email: epotma@uci.edu or eslee@kriss.re.kr.

This article contains supporting information online at https://www.pnas.org/lookup/suppl/doi:10.1073/pnas.1913729116/-/DCSupplemental.

First published December 11, 2019.

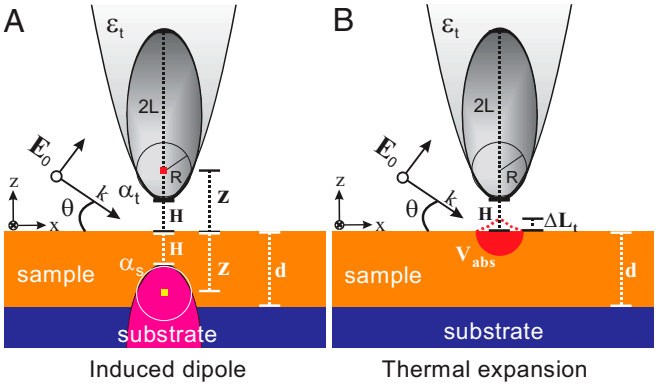

Fig. 1. Schematic diagram illustrating the (*A*) image dipole and the (*B*) tip-enhanced thermal expansion. The tip is modeled as an ellipsoid with a length of 2*L*. A plane wave illuminates the sample at an angle of θ. *H* is the gap distance from the tip end to the sample surface. α_t and α_s are the complex effective polarizabilities of the tip and the sample, respectively. *z* is the distance from the center of the dipole to the surface, V_{abs} is the absorption volume of the tip-enhanced field, and ΔL_t is the tip-enhanced thermal expansion.

and surface-localized nature of the heterodyne PiFM measurement by comparing it with other optomechanical force microcopy techniques such as the PTIR measurements and homodyne-detected PiFM (direct mode). Finally, we comprehensively address the origin of the spectroscopic forces—thermal versus dipole interaction—for the case where the 2 spectral responses coexist. A rigorous theoretical description and corresponding experimental demonstrations will be presented.

Results

Induced Dipole Force. We first examine the magnitude of the photoinduced dipole force for different sample materials and compare it to the magnitude of thermal expansion forces. Schematic diagrams of the induced dipole and the thermal expansion are sketched in Fig. 1 *A* and *B*, respectively. For the induced-dipole interaction, the light illumination induces dipoles in the tip and in the sample, which then mutually interact with each other. A coulombic force is present between the induced dipoles of the tip and the sample, which is given as follows (13, 23):

$$F_{dip}(z) \approx -\frac{3\mathrm{Re}\{\alpha_t^* \alpha_s\}}{2\pi\varepsilon_0 (2z)^4}|E_0|^2, \qquad [1]$$

where α_t and α_s are the complex effective polarizability of the tip and sample, respectively, within the point dipole approximation; *z* is the distance from the center of the dipole to the surface; and E_0 is the incident field. The spectral response is proportional to $\mathrm{Re}\{\alpha_t^* \alpha_s\} = \alpha_t' \alpha_s' + \alpha_t'' \alpha_s''$. Away from the tip's plasmonic resonance, where α_t' is nearly constant and $\alpha_t'' \sim 0$, the spectral line shape of the photoinduced force F_{dip} is dispersive near the molecular resonance of the sample (5, 20).

The induced dipoles exhibit both resonant and nonresonant contributions to the polarizability α_s. The nonresonant polarizability introduces a background in the frequency domain. For example, using the Clausius–Mossotti relation, the real part of the relative polarizability of polystyrene (PS) (α_{ps}) is around 0.42 relative to the polarizability of Au (α_{Au}) in the range between 1,380 cm^{-1} and 1,560 cm^{-1}, as shown in Fig. 2. The spectral response of α_{ps}' near the vibrational resonances of 1,454 and 1,492 of PS shows a dispersive lines shape (red dash line). The spectral variation of the resonance is one order of magnitude smaller than the nonresonant background value of 0.42. Consequently, the spectral contrast near the molecular resonance is limited, and thus difficult to measure in PiFM measurements, even if the total magnitude of F_{dip} is sufficiently above the noise level (5, 19, 24). The induced dipole force for a 60-nm PS film on a Si substrate is analytically calculated by implementing the finite dipole model (25, 26), indicated in Fig. 2 by the blue solid line. While the overall magnitude of F_{dip} constitutes a few piconewtons, which is within detectable limits, the spectral variation is in the sub-piconewton range, close to typical noise levels. Details of the computation are found in *SI Appendix*, section 1.

The nonresonant polarizability is related to the effective refractive index of the sample. For example, the induced dipole force can distinguish an Au nanowire (NW), which has no plasmonic resonance in the MIR range between 1,500 cm^{-1} and 1,750 cm^{-1}, from other dielectric materials based on the nonresonant polarizability. In Fig. 3*B*, the topography of a rectangular Au NW with a 200-nm width and a 50-nm height on a glass substrate is shown. In the 1,500 to 1,750 cm^{-1} range, the effective refractive index of the Au NW is around 2.0 to 2.7, while that of glass is around 1.2 to 1.3. At 1,500 cm^{-1}, where there is no plasmonic resonance of the Au NW nor a spectral resonance of the glass substrate, the F_{dip} on the Au NW is around 3 times greater than that on the glass substrate. The Au NW is successfully visualized on the glass substrate at 1,600 cm^{-1} and at 1,500 cm^{-1} with the induced dipole force, as shown in Fig. 3 *C* and *D*, respectively. The spectral dependence of the power-normalized photoinduced force in the range between 1,500 cm^{-1} and 1,750 cm^{-1} is nearly flat for both the Au NW and the glass substrate, as is evident from Fig. 3*E*.

Thermal Expansion Force. The latter experiments indicate that, although the induced dipole force provides sufficient contrast to discriminate different materials based on their MIR polarizabilities, the same photoinduced force is insufficient for resolving the polarizabilities associated with fundamental vibrational transitions in molecular samples above practical noise levels. Near molecular resonances, there is a temperature rise of the sample due to light absorption, which results in strain deformation of the sample that eventually gives rise to thermal expansion (11). The strong field enhancement in the tip–sample junction not only enhances the induced dipole moment but also increases the absorption of MIR light by the sample (15). The diagram illustrating the thermal response to incident light absorption is given in Fig. 1*B*. The thermal expansion (ΔL) couples to the tip through the gradient of the tip–sample intermolecular force (F_{ts}). In the small oscillation limit, the thermal expansion force between the tip and the sample is given as follows (27):

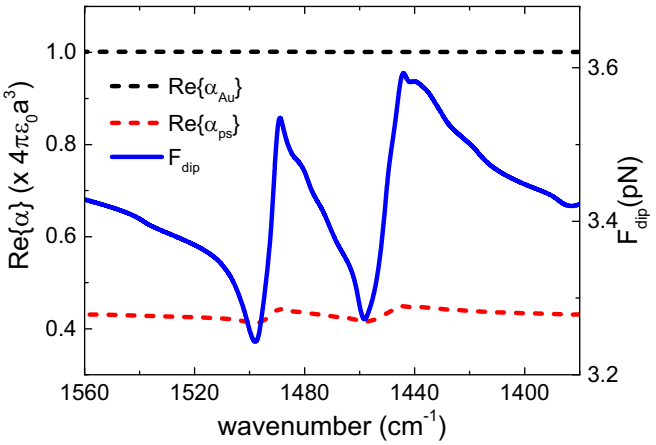

Fig. 2. Normalized real part of polarizabilities of Au (black dashed line) and PS (red dashed line) based on the Clausius–Mossotti relation, and the induced dipole force by implementing the finite dipole method (blue solid line).

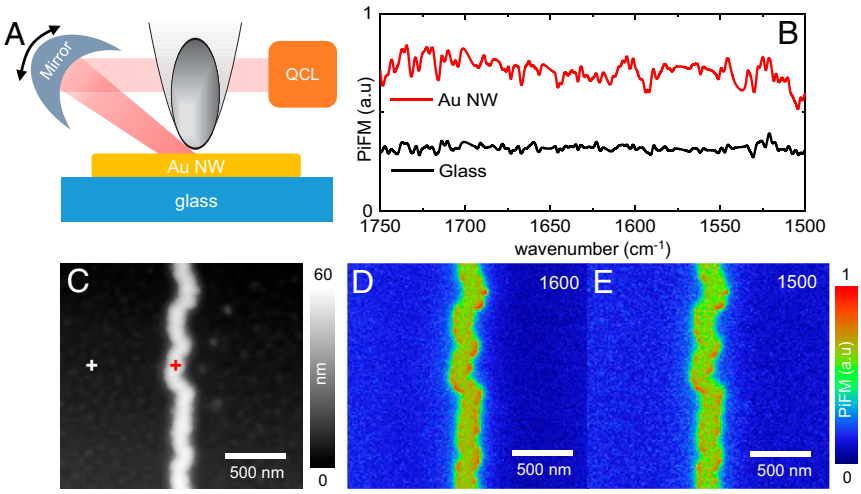

Fig. 3. Induced dipole force measurement in MIR PiFM. (*A*) Sketch of the photoinduced force measurement of an Au nanowire (NW) on a glass substrate by using a quantum cascade laser (QCL). (*B*) Spectral dependence of the power-normalized photoinduced force measured on the Au NW (red cross in topography) and on the glass (white cross in topography). (*C*) Topography and PiFM images at (*D*) 1,600 cm^{-1} and (*E*) 1,500 cm^{-1}.

$$F_{\text{th}}(z) \approx \frac{\partial F_{\text{ts}}}{\partial z} \Delta L(z), \qquad [2]$$

with $\Delta L(z) \approx \sigma d \Delta T(z)$, where σ is the linear thermal expansion coefficient, d is the thickness of the sample, and ΔT is the temperature increase due to light absorption.

The crucial difference between the induced dipole force and the thermal expansion force is the dependence of the force with respect to the optical frequency. In Fig. 4, the calculated force spectra of F_{dip} (blue dash line) and F_{th} (red solid line), based on literature values of the optical constant of PS (28), are plotted along with the PiFM experimental results for the 60-nm PS film on a Si substrate. Rather than mimicking the induced dipole force, the PiFM data correspond remarkably well to the calculated F_{th}. The F_{dip} shows a relatively small spectral variation below a few hundred femtonewtons and the spectral shape is dispersive. On the other hand, the F_{th} shows relatively large spectral change of a few tens of piconewtons and the spectrum resembles a dissipative (absorptive) Lorentzian profile, which closely mimics the measured PiFM spectrum. Details of the calculation can be found in the *SI Appendix*, section 2.

Comparison of the induced dipole force and the thermal expansion force, as relevant to molecular vibrational resonances in the MIR, thus reveals that F_{th} dominates the observed spectroscopic contrast. We next focus on the nature of the thermal expansion force as measured in heterodyne PiFM experiments. Because the tip enhances the absorption in the near field, the thermal expansion in the tip–sample junction exhibits a characteristic behavior. The instantaneous thermal expansion can be considered as 2 forms of material expansion underneath the sharp metal tip, given as $\Delta L(z(t)) \approx \Delta L_{\text{t}}(z(t)) + \Delta L_{\text{g}}(t)$ (27), where ΔL_{t} is the tip-enhanced thermal expansion and where ΔL_{g} is the global thermal expansion. These 2 contributions rely on the fact that the sample experiences 2 kinds of optical fields; one is the tip-enhanced near field and the other is the unaltered (nonconfined) incident field. The field enhancement at the tip rapidly decreases near the sample surface so that the absorption volume is limited by the spatial extent of the near field underneath the tip, which determines the tip-enhanced thermal expansion (ΔL_{t}) and represents the surface-selective response. On the other hand, the global thermal expansion (ΔL_{g}), which directly absorbs the incident light, is irrelevant to the presence of the tip and represents the bulk response of the sample. The expansion mechanisms are illustrated in a simplified picture in Fig. 5*A*. These thermal expansion behaviors are usually not separable with the conventional contact mode PTIR technique. However, because PiFM is operated in the noncontact/tapping mode with the heterodyne method (side-band mode) (22), which modulates the light at the beating frequency between the 2 eigenmodes of the cantilever at $f_{\text{m}} = |f_2 \pm f|_1$ as sketched in Fig. 5*B*, the heterodyne PiFM signal can successfully separate the surface response from the bulk response (27). Further details on the thermal expansion dynamics in PiFM can be found in *SI Appendix*, section 3.

The $\Delta L_{\text{t}}(z)$ is generated at the side-band coupled frequency by coupling the incident light absorption at f_{m} with the motion of the tapping amplitude at f_2. As derived in *SI Appendix*, section 3, the modulation depth of $\Delta L_{\text{t}}(z)$ at f_{s} is a function of the noncontact/tapping amplitude of A_2, and is given as $\Delta L_{\text{t}}(z(f_{\text{s}})) \approx (\partial \Delta L(z(f_{\text{m}}))/\partial z) A_2(z(f_2))$. It decreases in the contact region because the tapping amplitude decreases. In Fig. 5*C*, the theoretically expected $\Delta L_{\text{t}}(z(f_{\text{s}}))$ is plotted with respect to the tip–sample distance. The dominant force mechanism is manifested in the noncontact region. Experimentally, the

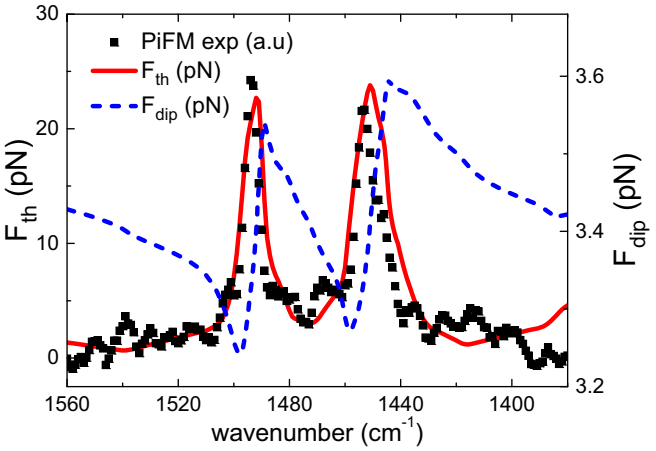

Fig. 4. Calculation of the induced dipole force (blue dash line) and the thermal expansion force (red solid line) along with the PiFM data (black square dots) for 60-nm PS on Si substrate.

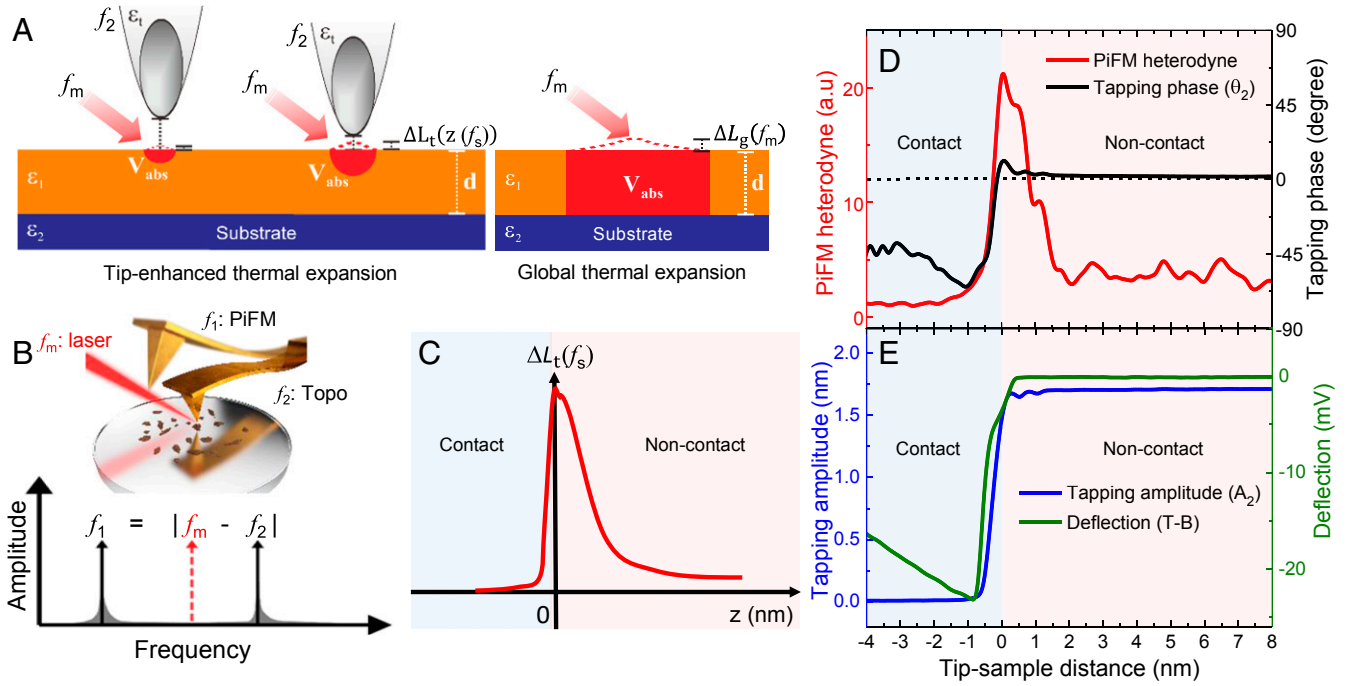

Fig. 5. Thermal expansion force measurement in PiFM. (*A*) Schematic diagram illustrating the tip-enhanced thermal expansion and the global thermal. (*B*) Schematic diagram of PiFM heterodyne (side-band mode) operation. (*C*) Illustrative tip-enhanced thermal expansion at the side-band coupled frequency with respect to the tip–sample distance. (*D*) PiFM heterodyne (red solid line), the tapping phase (black solid line), (*E*) the tapping amplitude (blue solid line), and the DC deflection (green solid line) with respect to the tip–sample distance.

noncontact region can be distinguished from the contact region in tapping mode PiFM by monitoring the phase shift of the tapping motion with respect to the tip–sample distance. When an attractive (or repulsive) force affects the tip, the tapping phase shifts toward positive (or negative) phase values relative to the interatomic force gradient. Fig. 5*D* shows the distance dependent heterodyne PiFM signal as measured on the 60-nm PS film at the 1,492 cm^{-1} vibrational resonance using a tapping amplitude under 1.7 nm. The heterodyne PiFM signal (red solid line) clearly increases in the noncontact region (positive tapping phase) and shows a maximum while it decreases in the contact region (negative tapping phase). Note that a positive tapping phase indicates the presence of a noncontact photoinduced force. The noncontact nature of the photoinduced thermal force is also demonstrated in another recent work (29), in which the photoinduced force dynamics are directly probed through the time-resolved peak force version of the photoinduced force microscope (pf-PiFM). Hence, the peak in Fig. 5*D* relates to the maximum position of pf-PiFM in the noncontact region. The simultaneously measured tapping amplitude (blue solid line) and mechanical DC deflection (green solid line) curves can be found in Fig. 5*E*. Note that the hard contact region starts near a tip–sample distance of −1 nm where the heterodyne PiFM signal disappears because the tapping amplitude goes to zero. In the heterodyne measurement, the tip-enhanced thermal expansion is dominated by the noncontact interatomic tip–sample force rather than the contact force or the photoacoustic mechanism, as was suggested in the previous work (21), because the signal vanishes in the contact region as well as in the region far away from the surface. *SI Appendix*, section 4 contains a deeper discussion of the noncontact nature of the heterodyne PiFM measurement.

Another interesting feature of the tip-enhanced thermal expansion force is its localized response to the sample surface, which shows a saturation rather than the continuous increase with respect to the sample thickness. The gap field enhancement between the tip and a high index substrate such as a Si wafer decreases with increasing thickness of the organic sample, PS, while the heating volume is proportional to the sample thickness. This results in a maximum in the tip-enhanced thermal expansion (ΔL_t) as a function of the sample thickness, as quantitatively calculated in the Fig. 6*B*. On the other hand, the global thermal expansion depends on the heating volume of the sample, so that it is directly proportional to the sample thickness until the focal volume. Note that, because the tip-enhanced thermal expansion is a localized response, the magnitude of the tip-enhanced thermal expansion is one order of magnitude smaller than the global thermal expansion in the thicker region. Thus, the total thermal expansion generally follows the global thermal expansion with respect to the thickness. The details of the diagram with a quantitative calculation can be found in *SI Appendix*, section 2. The ΔL_g response can be measured by homodyne-detected PiFM (direct mode) (23), which probes the total thermal expansion by directly modulating the light at the detection (fundamental) eigenmode of the cantilever as $f_m = f_1$.

To demonstrate the maximum behavior of the tip-enhanced thermal expansion force, we also examined a polymer wedge sample (Fig. 6*A*) made of PS on a Si substrate. The thickness of the PS layer ranges from a few tens of nanometers to a few hundreds of nanometers. The topographic image of the PS wedge is shown in Fig. 6*D*. The wedge is to the right side of the image, and some small debris of PS is found on the left side of the image, whose heights range from 30 to 40 nm. The heterodyne PiFM signal of the PS wedge at the 1,492 cm^{-1} IR vibrational resonance is obtained simultaneously and shown in Fig. 6*G*. The small debris is clearly imaged with a high signal-to-noise ratio, while the thick wedge shows a gradually decreased signal. To prove that the localized behavior is a unique characteristic for the heterodyne PiFM signal, we directly compare it with the homodyne PiFM signal and the PTIR signal of the PS wedge sample. Because both the homodyne-detected PiFM and PTIR probe the total thermal expansion, a continuously increasing signal behavior is expected. In Fig. 6 *H* and *I*, we observe that the homodyne PiFM and PTIR contrast gradually increase as a function of PS

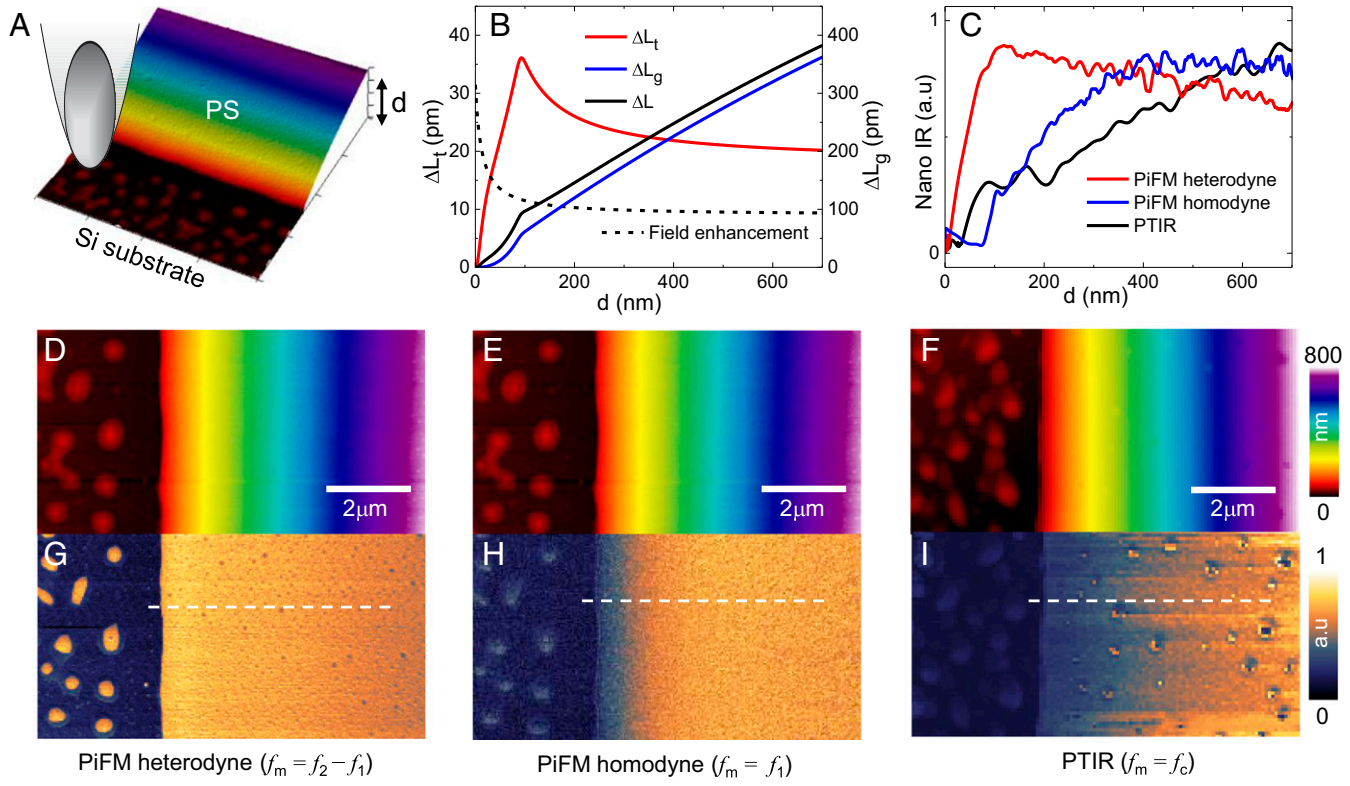

Fig. 6. Localized nature of PiFM heterodyne measurement compared to the PiFM homodyne and PTIR measurements. (*A*) Sketch of PS wedge on Si substrate for thickness-dependent PiFM measurements. (*B*) Theoretical expectation of the global thermal expansions as well as the field enhancement as a function of sample thickness. (*C*) Comparison between PiFM and PTIR response as a function of PS thickness as measured at the white dashed line cuts in *G–I*. (*D–I*) Nano-IR imaging of PS wedge at the PS vibrational resonance (1,492 cm^{-1}). (*G*) PiFM heterodyne, (*H*) PiFM homodyne, (*I*) PTIR, and corresponding topography (*D–F*), where the F_c is the contact force and f_c is the contact resonance.

thickness and the small debris is rarely visible. This is because ΔL_t is manifest predominantly on the subnanometer scale, even for a sample thickness of a few hundred nanometers, while ΔL_g may easily reach a scale one order of magnitude greater as shown in Fig. 6*B*. The line profiles at the white dashed lines in Fig. 6 *G–I* clearly show the maximum behavior of the heterodyne PiFM signal, while the homodyne PiFM signal and the PTIR response show a gradually increased response.

Mixed Case of Induced Dipole and Thermal Forces. The induced dipole contrast can be enhanced with the help of the tip-enhanced thermal expansion of a functionalized tip (30). It is well known that some commercial cantilevers may have a thin layer of polydimethylsiloxane (PDMS) contamination (1∼2 nm) on their surface, which can be traced to the packaging and shipping container (31, 32). Because the thermal expansion coefficient of PDMS is one order of magnitude larger than other polymers, the PDMS absorption at the tip end can generate additional strong tip–sample distance modulation by absorbing the enhanced field at the tip end despite its limited thickness. This can be regarded as a resonant enhancement of the induced dipole contrast (effective index "contrast", not the F_{dip} itself) through the tip-enhanced thermal expansion of the PDMS, because the field at the tip end is sensitive to the refractive index of the sample. Control experiments of the PiFM response with both the PDMS-functionalized tip and the PDMS-cleaned tip are thoroughly discussed in *SI Appendix*, sections 5 and 6.

Using a PDMS-functionalized tip, we study a case where the induced dipole and the thermal expansion contrasts are both relevant in the PiFM measurement. For this purpose, we consider an Au NW on a glass substrate that is partially covered with a tapered PS layer. In Fig. 7*C*, the sample is visualized in heterodyne PiFM mode while illuminated by radiation at 1,730 cm^{-1}, an energy far from absorption resonances of any materials. In the region where the Au NW is not covered by the PS layer, the Au is clearly resolved through the induced dipole force. The Au NW can be distinguished well up until a layer thickness of about 150 nm, which represents an enhanced subsurface probing depth relative to the previous work (∼60 nm) in the conventional scattering-type scanning near-field optical microscopy (33). Beyond this layer thickness, the near field at the tip apex is affected by the effective polarizability of the layered sample, which reduces the gap field amplitude, and thus suppresses the photoinduced force contributed by the presence of the gold material underneath.

In Fig. 7 *D–F*, the Au NW is mapped at different energies of the MIR light, producing images with remarkably different contrast. To understand these differences, it is helpful to study the Fourier-transform infrared spectroscopy (FTIR) spectra of the PS and glass materials, as well as the spectral response of the thin PDMS layer on the tip. The relevant spectra are shown in Fig. 7*G*, which are replotted from published results (28, 34, 35). At 1,492 cm^{-1}, PS has a strong vibrational absorption, whereas the other 2 materials show limited response at this energy. At 1,268 cm^{-1}, the strongest response is from PDMS. In the 1,000 to 1,100 cm^{-1} range, both the glass substrate and the PDMS layer exhibit vibrational resonances. Fig. 7*H* shows how the various vibrational resonances translate into changes in the PiFM signal. Here, PiFM spectra are taken at various points in Fig. 7*B*, indicated by 3 crosses. At the location of the red cross, where the tip is positioned on the glass, the red PiFM spectrum in Fig. 7*H* is obtained. The spectral response follows the FTIR spectrum of the PDMS layer on the tip. However, the photoinduced force

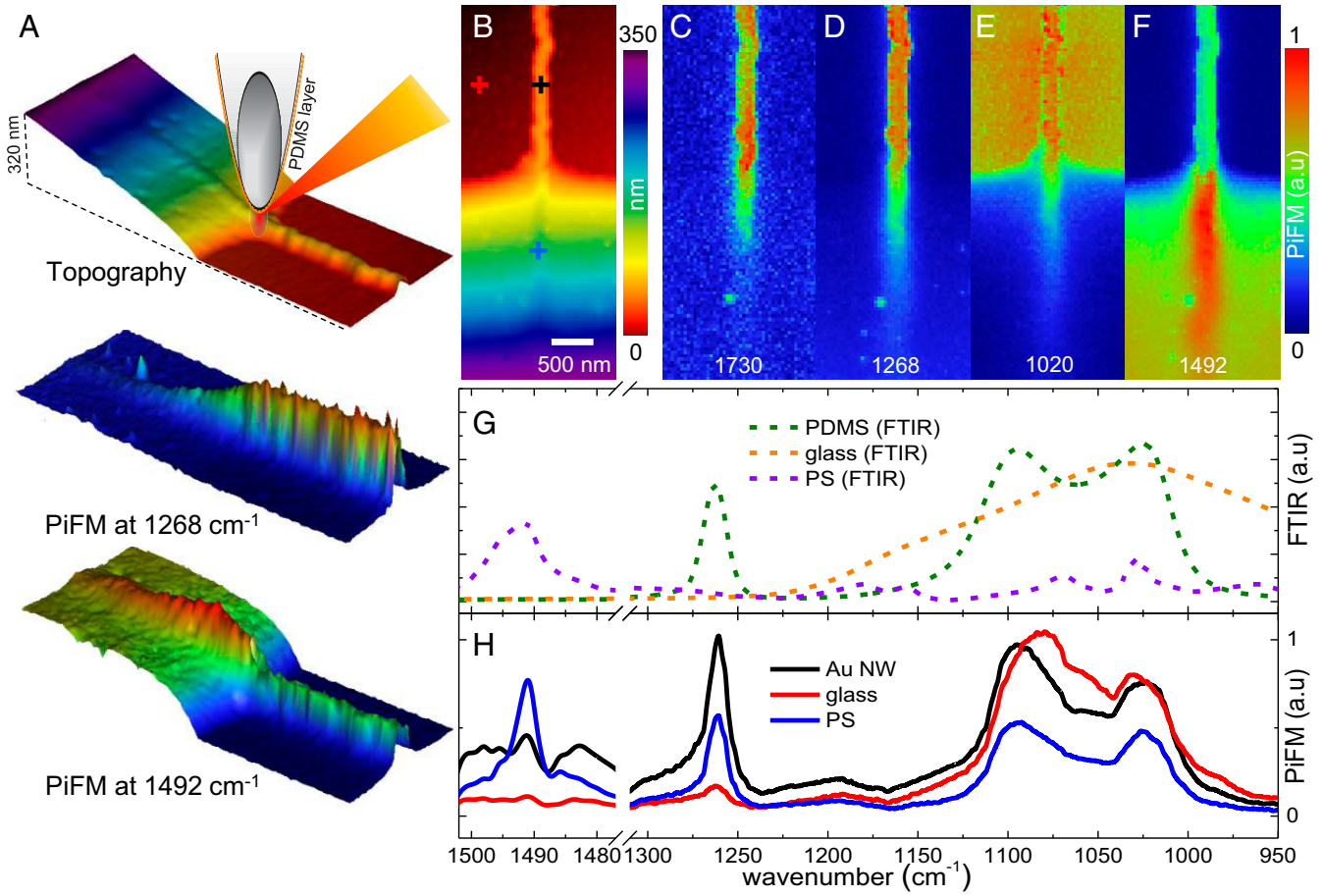

Fig. 7. Mixed case of the induced dipole and the tip-enhanced thermal expansion in the PiFM spectroscopic imaging for the buried Au NW under PS wedge on the glass substrate. (*A*) Sketch of the PDMS functionalized tip on the sample with 3D topography in *B*, 3D PiFM images in (*D*) 1,268 cm^{-1} and (*F*) 1,492 cm^{-1}. (*B–F*) Spectroscopic imaging of the buried Au NW under the PS wedge on glass substrate. (*B*) Topography and (*C*) PiFM images with the induced dipole force at 1,730 cm^{-1}, where there are no absorption resonances of PS, PDMS, glass, and Au NW. (*D*) Enhanced induced dipole contrast with the help of the tip-enhanced thermal expansion of the PDMS at the its vibrational resonance (1,268 cm^{-1}). (*E*) PiFM images of Au NW at the glass absorption (1,020 cm^{-1}) with the enhanced induced dipole contrast due to the functionalized tip. (*F*) PiFM image with the tip-enhanced thermal expansion of the PS wedge at the 1,492 cm^{-1} vibrational resonance with the dipole contrast. (*G*) FTIR spectra of the bulk PDMS (blue dashed line), glass (orange dashed line), and PS (violet dashed line) from the published results (34, 35). (*H*) PiFM spectra on the Au NW (black solid line), the glass substrate (red solid line), and the PS (blue solid line) at the black, red, and blue crosses in the topography, respectively.

grows stronger in the 1,000 to 1,100 cm^{-1} range, where the glass response is substantial. We thus see that the tip-enhanced thermal expansion force of the PDMS effectively enhances the response from the substrate underneath, in this case, glass.

When the tip is positioned on the Au NW, indicated by the black cross in Fig. 7*B*, we do not expect vibrational resonances from the gold. The PiFM spectrum again follows the spectral response of the PDMS layer, this time without an amplification of a particular region. The PiFM signal at a frequency off-resonance for glass is, however, significantly stronger when measured over the Au NW compared to when it is measured over glass. This reflects the magnitude of the gap field, which is significantly stronger in the case of gold, thus increasing the absorption of light energy by the PDMS layer. In addition, the induced dipole force F_{dip} is stronger over gold than it is over glass, which is reflective of their refractive index differences. Last, when the tip is positioned at the PS wedge (blue cross in Fig. 7*B*), the blue PiFM spectrum in Fig. 7*H* is observed. We see contributions from both the thermal expansion of the PS material as well as the PDMS layer on the tip.

With this spectral dependence in mind, we can now interpret the PiFM maps of Fig. 7 *D–F*. At 1,268 cm^{-1}, shown in Fig. 7*D*, PDMS has a strong vibrational resonance that enhances the photoinduced force signal over the Au NW. The image resembles that of Fig. 7*C*, however, the overall PiFM signal in Fig. 7*D* is much stronger with a relatively high signal-to-noise ratio and an enhanced subsurface probing depth of about 250-nm. Hence, by detecting the gold response through a vibrational resonance of PDMS, the effective photoinduced force is markedly enhanced. Because the force is based on the tip-enhanced thermal expansion of the PDMS, the force spectrum shows the absorptive Lorentzian shape of the PDMS, while the mapping produces the effective index map (induced dipole contrast) of the sample.

In Fig. 7*E*, the PiFM signal is measured at 1,020 cm^{-1}, where both the glass and the PDMS have a broad and strong absorption. The measured thermal expansion force over the glass is now comparable in magnitude to the PDMS-enhanced effective force signal over the gold. Consequently, in this range, PiFM mapping reveals limited contrast between the Au NW (refractive index contrast) and the glass substrate (thermal contrast). Note that the deposited Au NW can still be visualized inside the PS wedge by the effective index contrast as aided by the PDMS absorption.

At 1,492 cm^{-1}, the PiFM map shown in Fig. 7*F* is obtained. At this energy there are no absorption resonances except from PS. We may expect a contribution from the PS through the thermal expansion force. The glass and Au NW response at this energy, however, are governed by the PDMS-enhanced effective force

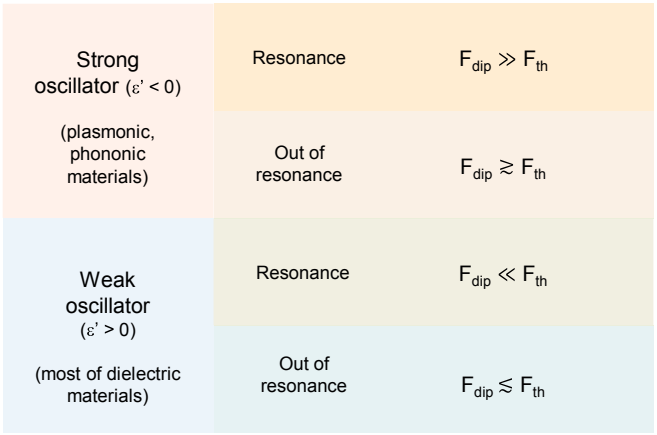

Fig. 8. Typical force comparison between the induced dipole force and the thermal expansion force with respect to material's properties.

signal. The Au NW is well resolved on the glass substrate, while the PS wedge shows the tip-enhanced thermal expansion behavior at 1,492 cm^{-1}. Note that because the tip-enhanced thermal expansion reflects the surface response, the PiFM heterodyne signal of the PS material on top of the Au NW shows a maximum as a function of PS thickness. Here, the maximum photoinduced force is found around 100 nm. Meanwhile, the PS material on top of the glass substrate rapidly saturates at a sample height of 70 nm. This is because the glass has a smaller refractive index (1.20) than the PS wedge (1.58), while the Au NW has a bigger index (2.69) in the MIR range. The gap field enhancement between the tip and the PS wedge increases with growing thickness of the PS material on the glass substrate while it decreases on the Au NW. This generates a different tip-enhanced thermal expansion response of the PS wedge, depending on the underlying substrate material, as is also evident from the 3D rendering obtained at 1,492 cm^{-1} and shown in Fig. 7*A*.

Discussion

We thus see that the induced dipole and the thermal expansion highly depend on the sample geometry and the material's properties. In Fig. 8, we present a comparison of the expected forces for different materials. The thermal expansion force is characterized by 3 material parameters: the absorption coefficient (a_{abs}), the relaxation time (τ_{rel}), and the thermal expansion coefficient (σ). The absorption coefficient increases at the molecular resonance, and thus the light energy is converted to heat, causing a temperature rise of the sample. The absorbed heat simultaneously undergoes a cooling process with respect to the relaxation time, $\tau_{rel} \approx 1.13(4/\pi^2)d^2/D$, which is related to the sample size (d) and the thermal diffusivity (D) (14, 27). Subsequently, the net accumulated heat deforms the sample to induce a thermal expansion determined by σ, which is related to the covalent bonding strength in the material. Materials with strong chemical bonds exhibit a smaller thermal expansion such as a crystalized metal structure. Thus, the thermal expansion force is usually dominant in most of dielectric materials (weak oscillator) near its molecular resonance and especially strong for linear polymer chains, which boast thermal expansion forces of a few hundred piconewtons even for a monolayer (15).

On the other hand, because the induced dipole force depends on the polarizability of a material, it is generally enhanced by noble metals, which have a high density of free electrons. The force is greatly enhanced for a strongly responsive oscillator such as a metal/inorganic polar crystal at plasmon/phonon polariton resonance where the permittivity is −1 or −2 (17, 36). Contrary to the strong oscillator, the magnitude of the polarizability change related to the weak oscillator near molecular vibrational resonance is one order of magnitude smaller than the nonresonant polarizability value. Because the magnitude of F_{dip} depends on both the polarizabilities of the metal tip and the sample, the force on the weak oscillator near a molecular resonance can be large in the range between a few piconewtons to a few tens of piconewtons (19, 37), while its spectral variation due to vibrational resonances is sub-piconewton. Because our system noise level is around 0.1 pN, the corresponding spectral variation for the dielectric materials is hardly detectable.

For the plasmonic materials, because of the low thermal properties (high D and low σ) of the metal, while the polarizability diverges near its resonance, the induced dipole force easily surpasses the thermal force. For example, a gold film on the glass substrate shows a strong field enhancement at the tip using P polarized light because of the excitation of surface plasmon polaritons (SPPs) (38), where the $\varepsilon' = -1$. The propagating SPP field distribution cannot be explained by the thermal expansion mechanism because the heat due to the SPPs is rapidly diffused on the Au film and the strong covalent bonds of the metal require more heat for their deformation. Besides that, Huang et al. and Tumkur et al. also successfully demonstrated that the dominant force for the plasmonic structure at its localized surface plasmon resonance is the induced dipole force by mapping the field distribution of the gold nanoparticle (36) and nanodisk (39). In the same manner, the induced dipole force observed from guided phonon polaritons of h-BN, which also has high D and low σ, produces distinct spatial maps of the guided phonon polaritons through their optical field gradient force (induced dipole force) (16).

In summary, we have shown, theoretically and experimentally, that both the induced dipole force (electromagnetic effect) and the tip-enhanced thermal expansion force (thermodynamic effect) of nanoscale materials contribute to the photoinduced force in the tip–sample junction. They are manifested simultaneously but have their own characteristic behaviors. For the induced dipole interaction, the tip induces an image dipole in the sample, which mutually interacts with the tip. The spectral dependence of the force follows the index of refraction so that its spectrum exhibits a dispersive line shape, which means that there is a nonresonant force even when the light energy is tuned off a molecular resonance. On the other hand, the thermal expansion force is the result of light absorption, which modulates the tip–sample distance through photothermal expansion, which eventually results in the modulation of the interatomic force. Because the force is based on the absorption of light quanta, the force spectrum follows the dissipative (absorptive) line shape. In the sense of "chemical" imaging, absorptive Lorentzian line shapes significantly facilitate the interpretation of the molecular response, and in this regard the photothermal response may be preferred over the induced dipole force. The induced dipole force may be valuable in the limit of chemical imaging, where the thermal expansion is minimal, i.e., in single-molecule imaging, as well as in field characterization of plasmonic/phononic materials. The insights obtained from this study can be applied to recent advances in optomechanical nanoscopy and spectroscopy to pursue the chemical characterization of heterogeneous nanobiomaterials as well as to reveal the nature of light–matter coupling in van der Waals materials.

Materials and Methods

Sample Preparation. The Au NW (height is 50 nm, and width is 200 nm) is synthesized by lithographically patterned NW electrodeposition (40) on soda lime glass. The 60-nm PS film is prepared by using the calibrated spin-coating method that the homopolymer PS is distributed onto Si substrate with respect to the revolutions per minute of the spin coater and the density of the PS (27). The PS wedge sample is prepared by the drop-and-dry method on a Si substrate.

PiFM Measurements. A VistaScope from Molecular Vista is used for the PiFM measurements. The microscope is coupled to a Laser Tune quantum cascade laser (QCL) system from Block Engineering with a tuning range from 800 to 1,800 cm^{-1} and a wave number resolution of 0.5 cm^{-1}. The sample is side-illuminated with the 40-ns pulsed beam at the 40° angle from the sample surface by a parabolic mirror that has the numerical aperture of around 0.4. The average illumination power of the QCL source is ∼5 mW with a 2λ diameter focal spot. The microscope is operated in noncontact/tapping mode with a gold-coated Si cantilever obtained from PPP-NCHAu from Nanosensors. The fundamental resonance is typically around 300 kHz, and the second resonance is around 1.88 MHz. The pulsed QCL beam is modulated by tuning its repetition rate to the difference frequency of cantilever's eigenmodes at $f_m = f_2 - f_1 = 1.58$ MHz. The free oscillating noncontact/tapping amplitude is typically around 1.5 nm at the second eigenmode of the cantilever and the experiment is performed at 88% of the free oscillating amplitude, where the phase is still positive, corresponding to the noncontact region.

PTIR Measurements. The resonance-enhanced PTIR measurement is conducted by using the contact mode of Vista-IR microscope, which tunes a repetition rate of Laser Tune QCL to a cantilever's contact resonance as $f_m = f_c$ (15, 27). PPP-FMAu from Nanosensors, a soft gold-coated Si cantilever, whose fundamental resonance is 69.8 kHz and stiffness is 3 N/m, is used for the measurements. The contact mode Vista-IR microscope demodulates the resonance-enhanced PTIR signal at the contact resonance of $f_c = 369$ kHz.

Sensitivity of a Cantilever in PiFM. The cantilever's force sensitivity at ith eigenmode derives from the thermal noise of it, given as $N_i = \sqrt{4K_B TBQ_i/\omega_i k_i}$, where ω_i, Q_i, and k_i are the resonance frequency, quality factor, and stiffness of the ith eigenmode of the cantilever, B is the system bandwidth, K_B is Boltzmann constant, and T is the absolute temperature. For the typical PPP-NCHAu (Nanosensors) parameters given as $\omega_1 = 2\pi \times 300$ kHz, $\omega_2 = 2\pi \times 18{,}800$ kHz, $Q_1 = 543$, $Q_2 = 697$, $k_1 = 37$ N/m, and $k_2 = 1{,}454$ N/m, the thermal noises for the fundamental and the second eigenmodes are found as $N_1 \approx 1.13$ pm and $N_2 \approx 0.08$ pm, where $B = 10$ Hz and $T = 300$ K, respectively. The minimum detectable forces, which correspond to the PiFM force sensitivity, given as $F_{\min_i} = k_i N_i$, are 0.08 and 0.17 pN for the fundamental and the second eigenmodes, respectively. For the typical PPP-FMAu (Nanosensors) parameters given as $\omega_1 = 2\pi \times 69.8$ kHz, $\omega_2 = 2\pi \times 437.6$ kHz, $Q_1 = 180$, $Q_2 = 300$, $k_1 = 3$ N/m, and $k_2 = 1{,}454$ N/m, the minimum detectable forces are 0.08 and 0.15 pN for the fundamental and the second eigenmodes, respectively.

Associated Content. The modeling of the induced dipoles and the force between tip and sample in the layered system is described in *SI Appendix*, section 1. The calculation details of the tip-enhanced thermal expansion force for 60-nm PS film on Si substrate is found in *SI Appendix*, section 2. The theory of PiFM heterodyne and PiFM homodyne for the thermal expansion at the tip–sample junction can be found in *SI Appendix*, section 3. The noncontact nature of the tip-enhanced thermal expansion in the PiFM heterodyne is discussed in *SI Appendix*, section 4. The PiFM and the PTIR spectrum on a clean empty ZnSe substrate with the same tip in the range between 900 and 1,350 cm^{-1} are described in *SI Appendix*, section 5. The PDMS-enhanced effective force response in PiFM is rigorously discussed with respect to the PDMS-functionalized/PDMS-cleaned tip in *SI Appendix*, section 6.

Data Availability. All data are included in the manuscript and *SI Appendix*.

ACKNOWLEDGMENTS. The authors thank to Dr. Xiaowei Li for the Au NW preparation. The authors also thank Molecular Vista, Inc., for the support of the system and the helpful discussions. This work was supported by the Korea Research Fellowship Program through the National Research Foundation of Korea funded by the Ministry of Science and Information and Communication Technology (2016H1D3A1938071). E.O.P. thanks the National Science Foundation (Grant CHE-1414466) for support.

1. A. Ashkin, Acceleration and trapping of particles by radiation pressure. *Phys. Rev. Lett.* **24**, 156–159 (1970).
2. D. Van Thourhout, J. Roels, Optomechanical device actuation through the optical gradient force. *Nat. Photonics* **4**, 211–217 (2010).
3. O. Ilic, H. A. Atwater, Self-stabilizing photonic levitation and propulsion of nanostructured macroscopic objects. *Nat. Photonics* **13**, 289–295 (2019).
4. J. Chen, J. Ng, Z. Lin, C. Chan, Optical pulling force. *Nat. Photonics* **5**, 531–534 (2011).
5. J. Jahng *et al.*, Linear and nonlinear optical spectroscopy at the nanoscale with photoinduced force microscopy. *Acc. Chem. Res.* **48**, 2671–2679 (2015).
6. H. D. Ou-Yang, M.-T. Wei, Complex fluids: Probing mechanical properties of biological systems with optical tweezers. *Annu. Rev. Phys. Chem.* **61**, 421–440 (2010).
7. Y. Zhao *et al.*, Nanoscopic control and quantification of enantioselective optical forces. *Nat. Nanotechnol.* **12**, 1055–1059 (2017).
8. A. Ashkin, J. M. Dziedzic, Optical trapping and manipulation of viruses and bacteria. *Science* **235**, 1517–1520 (1987).
9. A. Grigorenko, N. Roberts, M. Dickinson, Y. Zhang, Nanometric optical tweezers based on nanostructured substrates. *Nat. Photonics* **2**, 365–370 (2008).
10. D. Nowak *et al.*, Nanoscale chemical imaging by photoinduced force microscopy. *Sci. Adv.* **2**, e1501571 (2016).
11. A. Dazzi, C. B. Prater, AFM-IR: Technology and applications in nanoscale infrared spectroscopy and chemical imaging. *Chem. Rev.* **117**, 5146–5173 (2017).
12. L. Wang *et al.*, Nanoscale simultaneous chemical and mechanical imaging via peak force infrared microscopy. *Sci. Adv.* **3**, e1700255 (2017).
13. I. Rajapaksa, K. Uenal, H. K. Wickramasinghe, Image force microscopy of molecular resonance: A microscope principle. *Appl. Phys. Lett.* **97**, 073121 (2010).
14. J. Chae *et al.*, Nanophotonic atomic force microscope transducers enable chemical composition and thermal conductivity measurements at the nanoscale. *Nano Lett.* **17**, 5587–5594 (2017).
15. F. Lu, M. Jin, M. A. Belkin, Tip-enhanced infrared nanospectroscopy via molecular expansion force detection. *Nat. Photonics* **8**, 307–312 (2014).
16. A. Ambrosio *et al.*, Selective excitation and imaging of ultraslow phonon polaritons in thin hexagonal boron nitride crystals. *Light Sci. Appl.* **7**, 27 (2018).
17. M. Tamagnone *et al.*, Ultra-confined mid-infrared resonant phonon polaritons in van der Waals nanostructures. *Sci. Adv.* **4**, eaat7189 (2018).
18. Y. Huang *et al.*, Spectroscopic nanoimaging of all-semiconductor plasmonic gratings using photoinduced force and scattering type nanoscopy. *ACS Photonics* **5**, 4352–4359 (2018).
19. F. T. Ladani, E. O. Potma, Dyadic Green's function formalism for photoinduced forces in tip-sample nanojunctions. *Phys. Rev. B* **95**, 205440 (2017).
20. H. U. Yang, M. B. Raschke, Resonant optical gradient force interaction for nanoimaging and-spectroscopy. *New J. Phys.* **18**, 053042 (2016).
21. B. T. O'Callahan, J. Yan, F. Menges, E. A. Muller, M. B. Raschke, Photoinduced tip-sample forces for chemical nanoimaging and spectroscopy. *Nano Lett.* **18**, 5499–5505 (2018).
22. J. Jahng, B. Kim, E. S. Lee, E. O. Potma, Quantitative analysis of sideband coupling in photoinduced force microscopy. *Phys. Rev. B* **94**, 195407 (2016).
23. J. Jahng *et al.*, Gradient and scattering forces in photoinduced force microscopy. *Phys. Rev. B* **90**, 155417 (2014).
24. A. Ambrosio, R. C. Devlin, F. Capasso, W. L. Wilson, Observation of nanoscale refractive index contrast via photoinduced force microscopy. *ACS Photonics* **4**, 846–851 (2017).
25. A. Cvitkovic, N. Ocelic, R. Hillenbrand, Analytical model for quantitative prediction of material contrasts in scattering-type near-field optical microscopy. *Opt. Express* **15**, 8550–8565 (2007).
26. B. Hauer, A. P. Engelhardt, T. Taubner, Quasi-analytical model for scattering infrared near-field microscopy on layered systems. *Opt. Express* **20**, 13173–13188 (2012).
27. J. Jahng, E. O. Potma, E. S. Lee, Tip-enhanced thermal expansion force for nanoscale chemical imaging and spectroscopy in photoinduced force microscopy. *Anal. Chem.* **90**, 11054–11061 (2018).
28. V. Zolotarev, B. Volchek, E. Vlasova, Optical constants of industrial polymers in the IR region. *Opt. Spectrosc.* **101**, 716–723 (2006).
29. L. Wang, H. Wang, D. Vezenov, X. G. Xu, Direct measurement of photoinduced force for nanoscale infrared spectroscopy and chemical-sensitive imaging. *J. Phys. Chem. C* **122**, 23808–23813 (2018).
30. J. Jahng, H. Yang, E. S. Lee, Substructure imaging of heterogeneous nanomaterials with enhanced refractive index contrast by using a functionalized tip in photoinduced force microscopy. *Light Sci. Appl.* **7**, 73 (2018).
31. Y.-S. Lo *et al.*, Organic and inorganic contamination on commercial AFM cantilevers. *Langmuir* **15**, 6522–6526 (1999).
32. L. Sirghi, O. Kylián, D. Gilliland, G. Ceccone, F. Rossi, Cleaning and hydrophilization of atomic force microscopy silicon probes. *J. Phys. Chem. B* **110**, 25975–25981 (2006).
33. T. Taubner, F. Keilmann, R. Hillenbrand, Nanoscale-resolved subsurface imaging by scattering-type near-field optical microscopy. *Opt. Express* **13**, 8893–8899 (2005).
34. M. Querry, *Optical Constants of Minerals and Other Materials from the Millimeter to the Ultraviolet* (Chemical Research Development and Engineering Center Aberdeen Proving Groundmd, 1987).
35. M. Rubin, Optical properties of soda lime silica glasses. *Sol. Energy Mater.* **12**, 275–288 (1985).
36. F. Huang, V. A. Tamma, Z. Mardy, J. Burdett, H. K. Wickramasinghe, Imaging nanoscale electromagnetic near-field distributions using optical forces. *Sci. Rep.* **5**, 10610 (2015).
37. M. Almajhadi, H. K. Wickramasinghe, Contrast and imaging performance in photo induced force microscopy. *Opt. Express* **25**, 26923–26938 (2017).
38. J. Jahng *et al.*, Visualizing surface plasmon polaritons by their gradient force. *Opt. Lett.* **40**, 5058–5061 (2015).
39. T. U. Tumkur *et al.*, Photoinduced force mapping of plasmonic nanostructures. *Nano Lett.* **16**, 7942–7949 (2016).
40. X. Li, Y. Liu, J. C. Hemminger, R. M. Penner, Catalytically activated palladium@platinum nanowires for accelerated hydrogen gas detection. *ACS Nano* **9**, 3215–3225 (2015).